



Non-monotonic salt dependence of electro-osmotic flow in pH-regulated nanochannels

Mingyu Duan¹ , Luanzhe Xu¹ , Jiadong Chen¹  and Guang Chen¹ 

¹Department of Advanced Manufacturing and Robotics, College of Engineering, Peking University, Beijing, 100871, PR China

Corresponding author: Guang Chen, guangc@pku.edu.cn

(Received 9 October 2024; revised 2 December 2024; accepted 24 December 2024)

Electro-osmotic flow (EOF) in nanochannels exhibits a puzzling non-monotonic dependence on salt concentration, which contrasts with observations in microchannels and remains not fully understood. In this work, we address this phenomenon through a theoretical investigation of EOF in pH-regulated channels. New analytical approximations for electrostatic potential, EOF profile and electro-osmotic mobility beyond the Debye–Hückel limit are derived through asymptotic analysis. Our findings reveal that the surface electrostatic potential is independent of the channel size only when the half-channel size exceeds the Gouy–Chapman length. In contrast, surface ionization and net charge distribution play more crucial roles in EOF at the nanoscale, as they govern both the magnitude and the spatial distribution of the Coulomb driving force. As salt concentration increases, EOF velocity initially rises due to enhanced surface ionization, followed by a decline attributed to increased wall shear stress. This work provides key insights for EOF applications in nanofluidics and biomedical devices, and deepens the understanding of electrokinetic phenomena influenced by pH-regulation effects.

Key word: electrokinetic flows

1. Introduction

Electro-osmotic flow (EOF) is the motion of fluid induced by the movement of counterions near charged surfaces in response to an external electric field (Ajdari 1995; Squires & Bazant 2004; Bazant & Squires 2004; van der Heyden *et al.* 2006; Ghosal 2004). Owing to its feasibility for fluid manipulation at the micro/nanoscale (Stone, Stroock & Ajdari 2004; Schoch, Han & Renaud 2008; Zhao & Yang 2012; Bandopadhyay, Tripathi & Chakraborty 2016; Alizadeh *et al.* 2021), EOF has been widely exploited in various applications such

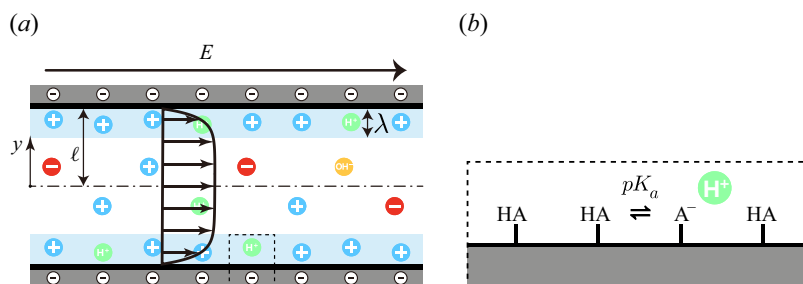


Figure 1. (a) Schematic of EOF triggered by an external electric field E applied along a negatively charged nanochannel, where ℓ and λ are the channel size and Debye length, respectively. (b) Zoomed-in view of the ionization equilibrium of the acidic groups HA at the channel walls.

as cell manipulation (Hui *et al.* 2016; Kounovsky-Shafer *et al.* 2017; Hur & Chung 2021), protein analysis (Das *et al.* 2012; Huang *et al.* 2017; Schmid *et al.* 2021), ionic valves (Chen & Das 2015; Koyama *et al.* 2021; Koyama *et al.* 2021) and seawater desalination (Picallo *et al.* 2013; Deng *et al.* 2015; Brown *et al.* 2021). Experimental studies have shown that in microchannels, the EOF velocity decreases with increasing salt concentration (Haywood, Harms & Jacobson 2014; Peng & Li 2016), which aligns with theoretical models assuming a constant surface charge density (Manning 1967; Chen & Das 2017). In contrast, within nanochannels, the EOF velocity initially increases and then decreases as the salt concentration rises (Pennathur & Santiago 2005; Haywood *et al.* 2014; Peng & Li 2016; Li & Li 2019). This non-monotonic behaviour is puzzling, as theories based on a constant surface charge density predict a plateau before the decrease, failing to explain the observed trends (Chen & Das 2017). It is important to note that the surface charge of a silica or polydimethylsiloxane (PDMS) channel is influenced by several factors including pH, salt concentration and channel size. This phenomenon is commonly referred to as surface charge regulation (Behrens & Grier 2001; Trefalt, Behrens & Borkovec 2016). Baldessari examined the effects of three different boundary conditions – specified surface potential, specified surface charge density and charge regulation – on the electric potential field and EOF in nanochannels, emphasizing the importance of achieving equilibrium between the channel and well (Baldessari 2008). Subsequent numerical studies of pH-regulated nanochannels have successfully captured this non-monotonic trend in EOF velocity with added salt (Liu, Tseng & Hsu 2015; Sadeghi, Saidi & Sadeghi 2017). However, the corresponding analytical expressions derived within the Debye–Hückel (DH) limit do not adequately explain the numerical or experimental data, as the pH-regulation effect becomes more pronounced beyond the DH limit (Duan *et al.* 2024).

We recently developed a new theoretical framework to investigate the influence of salt, confinement and pH on the surface charge density of carbon nanotubes, silica nanopores and colloidal nanoparticles (Duan *et al.* 2024). In this work, we examine the salt dependence of EOF in pH-regulated channels at both micro- and nanoscale. We present new predictions for the surface potential and the electro-osmotic mobility beyond the DH limit, and compare these predictions with experimental data. Our objective is to elucidate the non-monotonic dependence of EOF on salt concentration in pH-regulated nanochannels and to offer practical insights for surface potential measurements.

2. Theoretical model

We consider a two-dimensional channel of size 2ℓ (see figure 1a), where the channel walls are negatively charged due to the ionization of acidic groups, $\text{HA} \rightleftharpoons \text{A}^- + \text{H}^+$ (figure 1b).

Accordingly, the surface charge density σ is regulated by the hydrogen ion concentration at the surface, namely the surface pH value. The distributions of the electrostatic potential ψ and the ion concentrations n_i of various species $i = \pm, H^+, OH^-$ within the channel $-\ell \leq y \leq \ell$ can be obtained by solving the Poisson–Boltzmann (PB) equation:

$$\frac{d^2\psi}{dy^2} = -\frac{e}{\epsilon_0\epsilon_r} \sum_i z_i n_i, \tag{2.1a}$$

$$n_i = n_{i,\infty} \exp\left(-z_i \frac{e\psi}{k_B T}\right), \tag{2.1b}$$

with the boundary condition $d\psi/dy|_{y=\pm\ell} = \pm\sigma/(\epsilon_0\epsilon_r)$. Here, e is the elementary charge, k_B is the Boltzmann constant, T is the thermal temperature, ϵ_0 is the vacuum permittivity, ϵ_r is the relative permittivity of water, $z_i = \pm 1$ is the valence of the ion species, and $n_{i,\infty}$ is the bulk ion concentration. For an acidic solution ($\text{pH} \leq 7$), such as one prepared by adding HCl to a NaCl solution, the bulk ion concentrations are given by $n_{+,\infty} = n_s$, $n_{-,\infty} = n_s + n_{H^+,\infty} - n_{OH^-,\infty}$, $n_{H^+,\infty} = 10^3 N_A 10^{-\text{pH}}$ and $n_{OH^-,\infty} = 10^3 N_A 10^{-14+\text{pH}}$, where $N_A = 6.022 \times 10^{23}$ is the Avogadro constant. Thus, the degree of ionization σ/σ_0 of the charged surfaces is related to the undetermined surface electrostatic potential $\psi_S = \psi|_{y=\pm\ell}$:

$$\frac{\sigma}{\sigma_0} = \frac{1}{1 + 10^{\text{p}K_a - \text{pH}} \exp\left(-\frac{e\psi_S}{k_B T}\right)}, \tag{2.2}$$

where σ_0 is the maximum surface charge density and $\text{p}K_a$ is the ionization constant of the acidic groups (Duan *et al.* 2024).

When an external electric field E is applied along the channel, the Coulomb force acting on the mobile ions triggers EOF. The EOF velocity u can be determined using the Stokes equation

$$\eta \frac{d^2u}{dy^2} + Ee \sum_i z_i n_i = 0, \tag{2.3}$$

with a no-slip boundary condition $u|_{y=\pm\ell} = 0$, where η is the dynamic viscosity of the electrolyte solution (Burgreen & Nakache 1964). Accordingly, the electro-osmotic mobility μ_{eo} is defined as

$$\mu_{eo} = \frac{1}{2\ell E} \int_{-\ell}^{\ell} u \, dy. \tag{2.4}$$

Now, using (2.1)–(2.4), we can theoretically predict the distributions of the electrostatic potential ψ , ion concentration n_i , EOF velocity u and electro-osmotic mobility μ_{eo} in both micro- and nanochannels, and make comparisons with experiments.

3. Asymptotic analysis

3.1. Puzzling experimental observations

The aforementioned puzzling observations are illustrated in figure 2(a), where markers depict the experimental measurements of the electro-osmotic mobility μ_{eo} in borosilicate glass channels at various NaCl concentrations n_s where $\text{pH} \approx 5.5$ (Haywood *et al.* 2014). In the microchannel with a half-channel size of $\ell = 2500$ nm, the data represented by the blue markers show that μ_{eo} decreases monotonically as n_s increases. In contrast, nanochannels with $\ell = 108, 54$ and 27 nm exhibit non-monotonic behaviour, where μ_{eo}

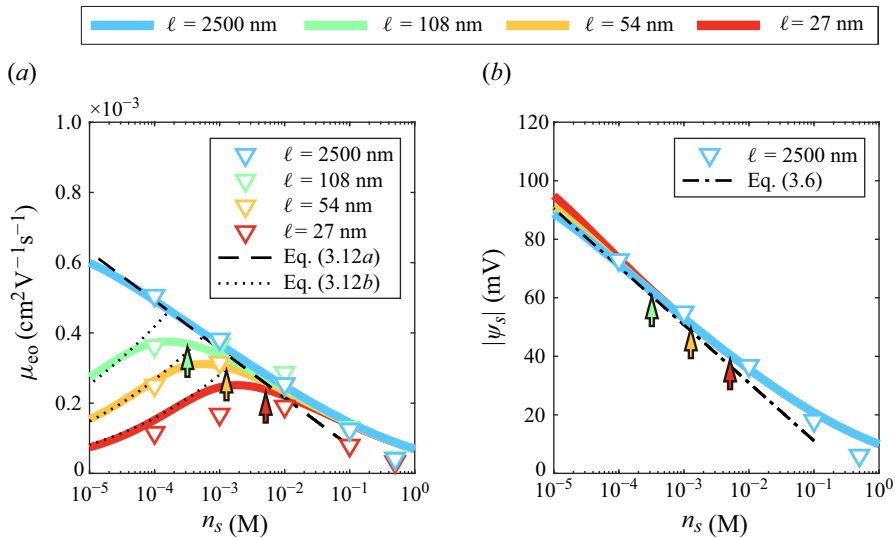


Figure 2. (a) Electro-osmotic mobility μ_{eo} and (b) surface electrostatic potential $|\psi_S|$ as functions of n_s . The triangle markers represent the experimental data measured in borosilicate glass micro/nanochannels where $\text{pH} \approx 5.5$ (Haywood *et al.* 2014). The coloured lines are the numerical predictions using $\epsilon_0 = 8.8 \times 10^{-12} \text{ F m}^{-1}$, $\epsilon_r = 80$, $k_B = 1.3804 \times 10^{-23} \text{ J K}^{-1}$, $T = 300 \text{ K}$, $\text{pH} = 5.5$, $\text{p}K_a = 6.6$ and $\sigma_0 = -0.45 \text{ C m}^{-2}$. The coloured arrows mark the positions where $\lambda = \ell / (2\pi)$ for the corresponding curves.

initially increases and then decreases with increasing n_s , as indicated by the green, yellow and red markers, respectively.

To further understand this phenomenon, we look into the corresponding surface electrostatic potential $|\psi_S|$ measured for $\ell = 2500 \text{ nm}$ at various n_s , as depicted by the blue markers in figure 2(b) (Haywood *et al.* 2014). The results indicate that $|\psi_S|$ decreases with increasing n_s , with data points for $n_s < 10^{-1} \text{ M}$ exceeding the DH limit, i.e. $|\psi_S| > k_B T / e$. Here, we have $k_B T / e \approx 25 \text{ mV}$, considering $k_B = 1.3804 \times 10^{-23} \text{ J K}^{-1}$, $T = 300 \text{ K}$ and $e = 1.6 \times 10^{-19} \text{ C}$. Apparently, previous theoretical predictions derived within the DH limit are not applicable (Liu *et al.* 2015; Sadeghi *et al.* 2017). Furthermore, we note that the Gouy–Chapman length $\ell_{GC} = 2\epsilon_0\epsilon_r k_B T / (e|\sigma|)$, which is less than 18 nm considering $|\sigma| > 0.002 \text{ C m}^{-2}$ for typical glass surfaces in contact with aqueous solutions, is significantly smaller than the half-channel size ℓ . Consequently, we can derive analytical approximations for ψ_S and μ_{eo} under the conditions of $|\psi_S| \gg k_B T / e$ and $\ell_{GC} \ll \ell$.

3.2. Analytical predictions for the electrostatic potential

The analytical predictions for the distributions of the electrostatic potential can be obtained using (2.1) and (2.2). The dimensionless forms of (2.1) and (2.2) and the corresponding boundary conditions are

$$\frac{d^2\psi}{d\bar{y}^2} = \frac{\sinh \psi}{\bar{\lambda}^2}, \quad \text{boundary conditions} \quad \left. \frac{d\psi}{d\bar{y}} \right|_{\bar{y}=\pm 1} = \pm \frac{\bar{\sigma}}{\bar{\lambda}^2}, \quad (3.1)$$

$$\frac{\sigma}{\sigma_0} = \frac{1}{1 + 10^{\text{p}K_a - \text{pH}} \exp(-\psi_S)}, \quad (3.2)$$

where the dimensionless parameters are $\Psi = e\psi/(k_B T)$, $\Psi_S = e\psi_S/(k_B T)$, $\bar{y} = y/\ell$, $\bar{\sigma} = \sigma/(\sum_i n_{i,\infty} e\ell)$ and $\bar{\lambda} = \lambda/\ell$, with $\lambda = \sqrt{\epsilon_0 \epsilon_r k_B T / (e^2 \sum_i n_{i,\infty})}$ being the Debye length which characterizes the thickness of the electric double layer (EDL).

Considering $|\Psi_S| \gg 1$ and $|\bar{\sigma}|/(2\bar{\lambda}^2) \gg 1$, or equivalently $|\psi_S| \gg k_B T/e$ and $\ell_{GC} \ll \ell$, the analytical approximation for the degree of ionization is derived as

$$\frac{\sigma}{\sigma_0} \approx \left(\frac{\bar{\lambda}^2}{10^{pK_a - pH} \bar{\sigma}_0^2} \right)^{\frac{1}{3}}, \tag{3.3}$$

where $\bar{\sigma}_0 = \sigma_0/(\sum_i n_{i,\infty} e\ell)$.

Accordingly, the electrostatic potential distributions are

$$\begin{aligned} \Psi(\bar{y}) \approx & 4 \tanh^{-1} \left[\frac{1 + \bar{\sigma}/\bar{\lambda}}{1 - \bar{\sigma}/\bar{\lambda}} \exp\left(\frac{-\bar{y} - 1}{\bar{\lambda}}\right) \right] \\ & + 4 \tanh^{-1} \left[\frac{1 + \bar{\sigma}/\bar{\lambda}}{1 - \bar{\sigma}/\bar{\lambda}} \exp\left(\frac{\bar{y} - 1}{\bar{\lambda}}\right) \right] \quad \text{for } |\Psi_C| \ll 1. \end{aligned} \tag{3.4a}$$

$$\Psi(\bar{y}) \approx -\ln \left(\frac{\pi^2 \bar{\lambda}^2}{(1 - 2\bar{\lambda}^2/\bar{\sigma})^2} \left[1 + \tan^2 \left(\frac{\pi \bar{y}}{2 - 4\bar{\lambda}^2/\bar{\sigma}} \right) \right] \right) \quad \text{for } |\Psi_C| \gg 1, \tag{3.4b}$$

where $\Psi_C = e\psi_C/(k_B T)$ and $\psi_C = \psi|_{y=0}$. The detailed derivations for (3.3), (3.4a) and (3.4b) are provided in Appendix A.

Both (3.4a) and (3.4b) lead to the same analytical prediction of the surface electrostatic potential,

$$\Psi_S \approx -\ln \left(\frac{\bar{\sigma}^2}{\bar{\lambda}^2} \right), \tag{3.5}$$

which is the same as (A3) and (A8) in Appendix A. Considering $n_s \gg n_{H^+, \infty}$, (3.5) can be simplified to

$$\left| \frac{e\psi_S}{k_B T} \right| \approx \frac{2}{3} \ln \left[\frac{|\sigma_0|}{e 10^{pK_a - pH}} \left(\frac{n_s}{2\pi \ell_B} \right)^{-\frac{1}{2}} \right], \tag{3.6}$$

where $\ell_B = e^2/(4\pi\epsilon_0\epsilon_r k_B T)$ is the Bjerrum length.

3.3. Analytical predictions for EOF

The analytical predictions for the distributions of EOF velocity can be obtained using (2.3). The dimensionless forms of (2.3) and the corresponding boundary conditions are

$$\frac{d^2 \bar{u}}{d\bar{y}^2} = \frac{\sinh \Psi}{\bar{\lambda}^2}, \quad \text{boundary conditions } \left. \frac{d\bar{u}}{d\bar{y}} \right|_{\bar{y}=\pm 1} = 0, \tag{3.7}$$

where $\bar{u} = u/u_0$ and $u_0 = E\epsilon_0\epsilon_r k_B T/(e\eta)$.

Combining (3.1) and (3.7) yields

$$\bar{u}(\bar{y}) = \Psi - \Psi_S. \tag{3.8}$$

Substituting (3.4a) and (3.5) into (3.8) yields

$$\bar{u}(\bar{y}) \approx 4 \tanh^{-1} \left[\frac{1 + \bar{\sigma}/\bar{\lambda}}{1 - \bar{\sigma}/\bar{\lambda}} \exp\left(\frac{-\bar{y} - 1}{\bar{\lambda}}\right) \right] + 4 \tanh^{-1} \left[\frac{1 + \bar{\sigma}/\bar{\lambda}}{1 - \bar{\sigma}/\bar{\lambda}} \exp\left(\frac{\bar{y} - 1}{\bar{\lambda}}\right) \right] + \ln\left(\frac{\bar{\sigma}^2}{\bar{\lambda}^2}\right) \quad \text{for } |\Psi_C| \ll 1, \quad (3.9a)$$

$$\bar{u}(\bar{y}) \approx \ln \left[\frac{1 + \tan^2\left(\frac{\pi}{2-4\bar{\lambda}^2/\bar{\sigma}}\right)}{1 + \tan^2\left(\frac{\pi\bar{y}}{2-4\bar{\lambda}^2/\bar{\sigma}}\right)} \right] \quad \text{for } |\Psi_C| \gg 1. \quad (3.9b)$$

Finally, substituting (3.9a) and (3.9b) into (2.4), the analytical predictions for the electro-osmotic mobility μ_{eo} are obtained:

$$\frac{\mu_{eo}}{\mu_0} \approx \frac{2}{3} \ln \left(\frac{|\bar{\sigma}_0|}{10^{pK_a - \text{pH}} \bar{\lambda}} \right) \quad \text{for } |\Psi_C| \ll 1, \quad (3.10a)$$

$$\frac{\mu_{eo}}{\mu_0} \approx 2 \ln \left[\frac{1}{2\pi \bar{\lambda}} \left(\frac{|\bar{\sigma}_0|}{10^{pK_a - \text{pH}} \bar{\lambda}} \right)^{\frac{1}{3}} + 1 \right] \quad \text{for } |\Psi_C| \gg 1, \quad (3.10b)$$

where $\mu_0 = \epsilon_0 \epsilon_r k_B T / (e\eta)$ is introduced for normalization. The threshold $|\Psi_C| \approx 1$ is equivalent to

$$\lambda \approx \frac{\ell}{2\pi}, \quad (3.11)$$

which is obtained analytically by determining the intersection point of (3.10a) and (3.10b). Considering $n_s \gg n_{H+, \infty}$, (3.10a) and (3.10b) can be simplified to

$$\frac{\mu_{eo}}{\mu_0} \approx \frac{2}{3} \ln \left[\frac{|\sigma_0|}{e 10^{pK_a - \text{pH}}} \left(\frac{n_s}{2\pi \ell_B} \right)^{-\frac{1}{2}} \right] \quad \text{for } \lambda \ll \frac{\ell}{2\pi}, \quad (3.12a)$$

$$\frac{\mu_{eo}}{\mu_0} \approx 2 \ln \left[\left(\frac{4\ell_B^2 |\sigma_0| n_s \ell^3}{\pi e 10^{pK_a - \text{pH}}} \right)^{\frac{1}{3}} + 1 \right] \quad \text{for } \lambda \gg \frac{\ell}{2\pi}. \quad (3.12b)$$

Here, combining (3.6) and (3.12a), we obtain $\mu_{eo}/\mu_0 = e|\psi_S|/(k_B T)$, which aligns with the Helmholtz–Smoluchowski (HS) theory. In contrast, when the Debye length becomes larger than the channel size, i.e. $\lambda \gg \ell/(2\pi)$, the ratio μ_{eo}/μ_0 becomes a function of ℓ , as indicated in (3.12b).

3.4. Fitting parameters

It is important to note that two key parameters, the maximum surface charge density σ_0 and the ionization constant pK_a of the charged surfaces, are not provided in the referenced article (Haywood *et al.* 2014). To determine these parameters, we first fit the experimental data for $|\psi_S|$ shown in figure 2(b) using (3.6). The fitting process yields $\sigma_0 = -0.45 \text{ C m}^{-2}$ and $pK_a = 6.6$, which are consistent with ranges reported in previous studies on glass–water interfaces (Sjöberg 1996; Mueller *et al.* 2003). Using these fitted values, we compute the numerical predictions of $|\psi_S|$ for various values of ℓ , as shown by the coloured lines in figure 2(b), which exhibit close alignment. We then calculate the corresponding numerical predictions of μ_{eo} for various values of ℓ , as represented by the coloured lines in figure 2(a). These predictions fit well with both the experimental data and the theoretical predictions from (3.12a) and (3.12b) in the corresponding regimes.

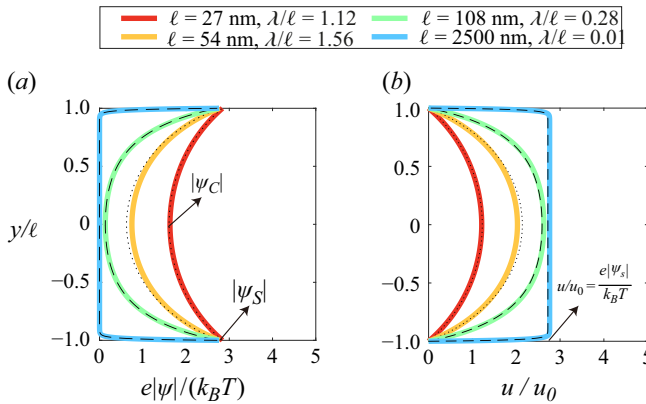


Figure 3. (a) Numerical predictions for the spatial distributions of dimensionless electrostatic potential $e|\psi|/(k_B T)$ with various ℓ considering $n_s = 10^{-4}$ M (or equivalently $\lambda = 30.2$ nm), where the dashed and dotted lines are the corresponding analytical predictions using (3.4a) and (3.4b), respectively. (b) Numerical predictions for the dimensionless EOF velocity u/u_0 with various ℓ considering $n_s = 10^{-4}$ M (or equivalently $\lambda = 30.2$ nm), where the dashed and dotted lines are the corresponding analytical predictions using (3.9a) and (3.9b), respectively. Other parameters are identical to those used in figure 2.

Notably, the results indicate that the HS theory is applicable only in microchannels or at high salt concentrations, provided the condition $\lambda \ll \ell/(2\pi)$ is satisfied.

4. Discussion

4.1. Influence of channel size

To clarify the effect of channel size on EOF, we present the predicted distributions of the dimensionless electrostatic potential $e|\psi|/(k_B T)$ and EOF velocity u/u_0 within the channel at $n_s = 10^{-4}$ M for various ℓ in figure 3(a,b), respectively. The Debye length λ is approximately 30 nm, remaining constant for $n_s = 10^{-4}$ M and pH = 5.5. Figure 3(a) shows that while the centre electrostatic potential $|\psi_C|$ increases as ℓ decreases, the surface electrostatic potential $|\psi_S|$ remains independent of ℓ . This behaviour arises because the analysed cases fall within the regime where $\ell_{GC} \ll \ell$. According to (2.2), the surface charge density σ is also unaffected by ℓ , ensuring that the total net charge $\int_{-\ell}^{\ell} n_{net} dy$ remains constant due to electroneutrality, where $n_{net} = \sum_i z_i n_i$ represents the net charge density. As ℓ decreases to the order of λ , the EDLs on both sides of the channel generally converge, leading to an increase in $|\psi_C|$. In figure 3(b), a plug-like velocity profile is shown for the EOF velocity u/u_0 in the microchannel with $\ell = 2500$ nm. This occurs because the driving Coulomb force of the EOF is concentrated within the EDL, the length scale of which is significantly smaller than the half-channel size, i.e. $\lambda \ll \ell$ (Burgreen & Nakache 1964; Arulanandam & Li 2000). The plateau value can be captured by the HS equation $u = u_0 e|\psi_S|/(k_B T)$, which remains constant for even larger ℓ . In contrast, as ℓ approaches the scale of λ , the plug-like profile diminishes and u/u_0 decreases due to the increasing spatial confinement.

4.2. Influence of salt concentration

To elucidate the impact of salt concentration n_s on EOF in nanochannels, we visualize the distributions of net charge density n_{net} and dimensionless EOF velocity u/u_0 at different

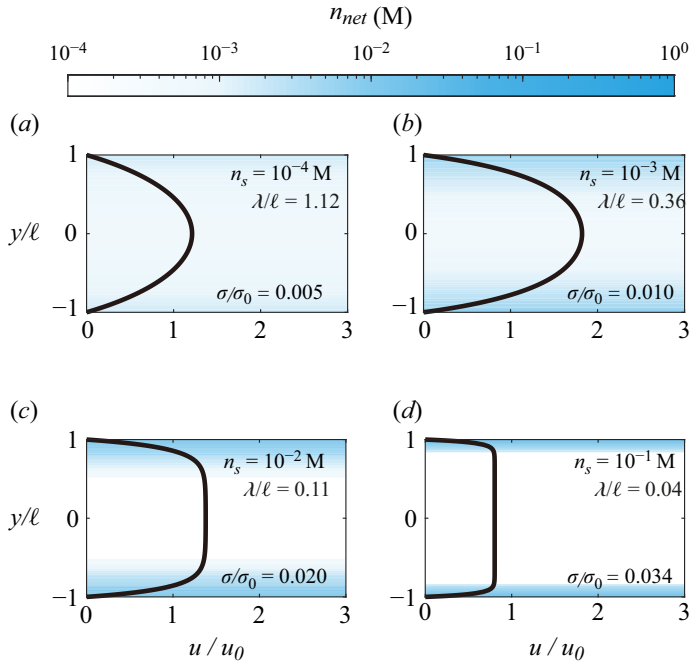


Figure 4. Numerical predictions for the spatial distributions of net charge density $n_{net} = n_+ - n_- + n_{H^+} - n_{OH^-}$ (colourmaps) and dimensionless EOF velocity u/u_0 (solid lines) in the nanochannel with $\ell = 27$ nm for various n_s . Numerical predictions for the degree of ionization σ/σ_0 at each n_s are marked in the corresponding subplot. Other parameters are identical with those used in figure 2.

n_s for $\ell = 27$ nm in figure 4. The degree of ionization σ/σ_0 for each case is indicated in the corner, showing an increase with the addition of salt due to the pH-regulation effect. At low salt concentrations, i.e. $n_s = 10^{-4}$ M and $n_s = 10^{-3}$ M as indicated in figure 4(a,b), wide diffusive layers are observed because the EDL thicknesses, i.e. $\lambda \approx 30$ nm and $\lambda \approx 10$ nm, respectively, are large compared with the half-channel size. Consequently, the driving Coulomb force of the EOF is evenly distributed across the channel, leading to parabolic-like velocity profiles. Meanwhile, as the degree of ionization σ/σ_0 for $n_s = 10^{-3}$ M is higher than that for $n_s = 10^{-4}$ M, the driving Coulomb force is stronger for $n_s = 10^{-3}$ M, resulting in a greater EOF rate compared with $n_s = 10^{-4}$ M. At high salt concentrations, i.e. $n_s = 10^{-2}$ M and $n_s = 10^{-1}$ M in figure 4(c,d), net charges predominantly accumulate near the walls, resulting in plug-like velocity profiles since the corresponding Debye lengths, i.e. $\lambda \approx 3$ nm and $\lambda \approx 1$ nm, respectively, are small compared with the half-channel size. Moreover, the EOF at $n_s = 10^{-1}$ M is more severely retarded due to wall shear stress, despite the degree of ionization σ/σ_0 and the driving Coulomb force being greater than those at $n_s = 10^{-2}$ M.

4.3. Potential effect of the Stern layer

The Stern layer is often considered a crucial factor in charge regulation, as it is assumed that the ions are tightly adsorbed to the charged surface, leading to a linear drop in electrostatic potential. Baldessari's model incorporates the Stern layer in its charge regulation boundary condition, expressed in our notation as

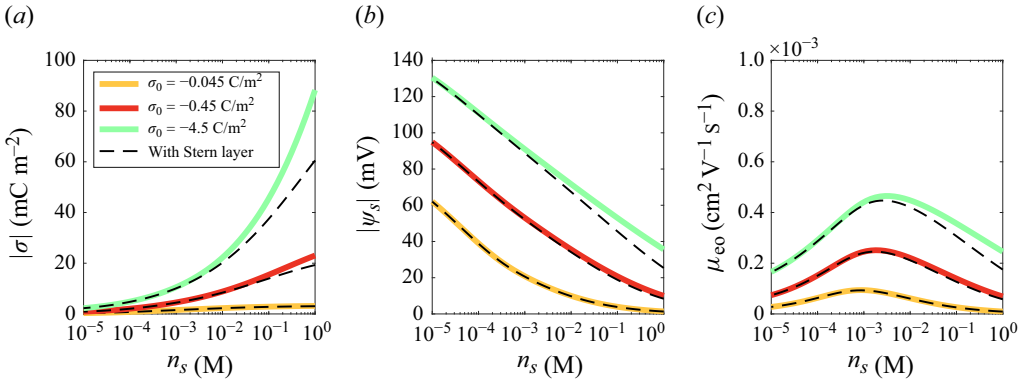


Figure 5. (a) Surface charge density $|\sigma|$, (b) surface electrostatic potential $|\psi_S|$ and (c) electro-osmotic mobility μ_{eo} as functions of n_s for different σ_0 . The solid lines represent the numerical predictions obtained from the boundary condition in (2.2). The dashed lines are the numerical predictions obtained from the boundary condition in (4.1) considering $C = 3.0 \text{ F m}^{-2}$, as reported in Baldessari (2008). Other parameters are identical to those used in figure 2.

$$\frac{\sigma}{\sigma_0} = \frac{1}{1 + 10^{\text{p}K_a - \text{pH}} \exp\left(-\frac{e\psi_S}{k_B T} - \frac{e\sigma}{Ck_B T}\right)}, \quad (4.1)$$

where σ/C is the potential drop within the Stern layer and C is the Stern layer’s phenomenological capacity (Behrens & Grier 2001; Baldessari 2008). To evaluate the potential effects of the Stern layer, we compare the numerical predictions for $|\sigma|$, $|\psi_S|$ and μ_{eo} using the two boundary conditions in (2.2) and (4.1), as shown in figure 5(a–c).

The results indicate that the two boundary conditions yield similar predictions for smaller surface group densities of $\sigma_0 = -0.045 \text{ C m}^{-2}$ and $\sigma_0 = -0.45 \text{ C m}^{-2}$. In contrast, for $\sigma_0 = -4.5 \text{ C m}^{-2}$, the model that incorporates the Stern layer predicts slightly lower values for $|\sigma|$, $|\psi_S|$ and μ_{eo} when $n_s > 10^{-2} \text{ M}$. Thus, we anticipate that incorporating the Stern layer is primarily necessary for surfaces with extensive chargeable groups.

4.4. Range of applicability of the classical PB equation

The classical PB equation is a well-established framework for modelling electrostatic interactions. While it may be regarded as less effective at very high salt concentrations due to factors such as ion size and ion–ion correlations, it remains a valid and robust approach for the specific cases presented in our study. Please note that the salt concentrations we consider, ranging from $n_s = 10^{-5}$ to 1 M, are significantly lower than the cutoff concentration $n_s^{cut} = a^{-3} = 5 \sim 60 \text{ M}$, considering a typical ion size of $a = 0.3 \sim 0.7 \text{ nm}$. This suggests that the ion size effect is negligible, thereby justifying the applicability of the classical PB equation (Storey *et al.* 2008). Furthermore, scenarios with salt concentrations exceeding 1 M are less relevant to this work, as both the EOF velocity and electro-osmotic mobility approach zero in these conditions.

5. Conclusion

In conclusion, when it comes to EOF at the nanoscale, the ionization of charged surfaces and the distribution of net charge across the channel emerge as more critical factors

than the surface potential, as they govern both the magnitude and the spatial distribution of the Coulomb driving force of the EOF. By analysing the experimental data, fitting them with our analytical predictions, and visualizing the electrostatic potential, net charge distribution and EOF velocity profile across the channel, we provide a comprehensive explanation for the non-monotonic salt dependence of the electro-osmotic mobility in pH-regulated nanochannels. Specifically, as the salt concentration increases, the initial rise of the electro-osmotic mobility is caused by the increase of surface charge density, while the subsequent decline is induced by the increase of the wall shear stress. Furthermore, we identify a transition point at $\lambda \approx \ell/(2\pi)$, where the EOF velocity shifts from a parabolic-like to a plug-like profile, which has practical implications for applications such as cell manipulations at the nanoscale. Additionally, we highlight that the Helmholtz–Smoluchowski theory is applicable only to microchannels or at high salt concentrations where $\lambda \ll \ell$, a limitation that may have been overlooked in zeta-potential measurement. We anticipate that this work will advance the understanding of EOF in nanofluidic systems, with applications ranging from particle separation and ionic valves to seawater desalination, while also providing new insights into broader electrokinetic phenomena influenced by pH regulation.

Funding. This work was supported by the National Natural Science Foundation of China (no. 12372259).

Declaration of interests. The authors report no conflict of interest.

Data availability statement. The data that support the findings of this study are available from the corresponding author upon reasonable request.

Appendix A. Analytical approximations of the electrostatic potential and degree of ionization

We first derive the analytical approximations of Ψ considering $|\Psi_S| \gg 1$ and $|\bar{\sigma}|/(2\bar{\lambda}^2) \gg 1$.

When $|\Psi_C| \ll 1$, integrating (3.1) from 0 to \bar{y} , using $\cosh \Psi_C \approx 1$ and considering the symmetry at $\bar{y} = 0$, i.e. $d\Psi/d\bar{y}|_{\bar{y}=0} = 0$, we have

$$\frac{1}{2} \left(\frac{d\Psi}{d\bar{y}} \right)^2 \approx \frac{\cosh \Psi - 1}{\bar{\lambda}^2}, \quad (\text{A1})$$

which yields an analytical solution,

$$\Psi(\bar{y}) \approx 4 \tanh^{-1} \left[C_1 \exp \left(\frac{-\bar{y} - 1}{\bar{\lambda}} \right) \right] + 4 \tanh^{-1} \left[C_1 \exp \left(\frac{\bar{y} - 1}{\bar{\lambda}} \right) \right], \quad (\text{A2})$$

where the constant C_1 needs to be determined. Using the boundary condition $d\Psi/d\bar{y}|_{\bar{y}=\pm 1} = \pm (\bar{\sigma}/\bar{\lambda}^2)$ in (A1), we obtain $\Psi_S \approx 2 \sinh^{-1}(\bar{\sigma}/2\bar{\lambda})$. Considering $|\Psi_S| \gg 1$, it can be simplified to

$$\Psi_S \approx -\ln \left(\frac{\bar{\sigma}^2}{\bar{\lambda}^2} \right). \quad (\text{A3})$$

Combining (A2) and (A3) gives $C_1 \approx (1 + \bar{\sigma}/\bar{\lambda})/(1 - \bar{\sigma}/\bar{\lambda})$. Substituting C_1 into (A2) yields

$$\Psi(\bar{y}) \approx 4 \tanh^{-1} \left[\frac{1 + \bar{\sigma}/\bar{\lambda}}{1 - \bar{\sigma}/\bar{\lambda}} \exp\left(\frac{-\bar{y} - 1}{\bar{\lambda}}\right) \right] + 4 \tanh^{-1} \left[\frac{1 + \bar{\sigma}/\bar{\lambda}}{1 - \bar{\sigma}/\bar{\lambda}} \exp\left(\frac{\bar{y} - 1}{\bar{\lambda}}\right) \right], \tag{A.4}$$

which is the same as (3.4a) in the main text.

When $|\Psi_C| \gg 1$, using $\sinh \Psi \approx \exp(-\Psi)/2$, (3.1) can be simplified to

$$\frac{d^2 \Psi}{d\bar{y}^2} \approx -\frac{\exp(-\Psi)}{2\bar{\lambda}^2}, \tag{A5}$$

which yields an analytical solution,

$$\Psi(\bar{y}) \approx -\ln \left(C_2 \bar{\lambda}^2 \left[1 + \tan^2 \left(\frac{\sqrt{C_2}}{2} \bar{y} \right) \right] \right), \tag{A6}$$

where the constant C_2 needs to be determined. Using the boundary condition $d\Psi/d\bar{y}|_{\bar{y}=\pm 1} = \pm \bar{\sigma}/\bar{\lambda}^2$ in (A6), we have $\sqrt{C_2}/2 \tan(\sqrt{C_2}/2) \approx -\bar{\sigma}/(2\bar{\lambda}^2)$, which leads to $C_2 \approx \pi^2/(1 - 2\bar{\lambda}^2/\bar{\sigma})^2$ considering $|\bar{\sigma}|/(2\bar{\lambda}^2) \gg 1$. Substituting C_2 into (A6) yields

$$\Psi(\bar{y}) \approx -\ln \left(\frac{\pi^2 \bar{\lambda}^2}{(1 - 2\bar{\lambda}^2/\bar{\sigma})^2} \left[1 + \tan^2 \left(\frac{\pi \bar{y}}{2 - 4\bar{\lambda}^2/\bar{\sigma}} \right) \right] \right), \tag{A7}$$

which is the same as (3.4b) in the main text. Equation (A7) further leads to

$$\Psi_S \approx -\ln \left(\frac{\bar{\sigma}^2}{\bar{\lambda}^2} \right). \tag{A8}$$

Note that (A3) and (A8) are identical. Thus, we can combine these two scenarios and probe σ/σ_0 for $|\Psi_S| \gg 1$ and $|\bar{\sigma}|/(2\bar{\lambda}^2) \gg 1$. Substituting (A3) or (A8) into (3.2) yields

$$\frac{\sigma}{\sigma_0} \approx \left(\frac{\bar{\lambda}^2}{\bar{\sigma}_0^2 10^{\text{p}K_a - \text{pH}}} \right)^{\frac{1}{3}} \left[\sqrt[3]{\frac{1}{2} \sqrt{1 + \frac{4\bar{\lambda}^2}{27\bar{\sigma}_0^2 10^{\text{p}K_a - \text{pH}}} + \frac{1}{2}}} - \sqrt[3]{\frac{1}{2} \sqrt{1 + \frac{4\bar{\lambda}^2}{27\bar{\sigma}_0^2 10^{\text{p}K_a - \text{pH}}} - \frac{1}{2}}} \right]. \tag{A9}$$

Equation (A9) can be further simplified to

$$\frac{\sigma}{\sigma_0} \approx \left(\frac{\bar{\lambda}^2}{10^{\text{p}K_a - \text{pH}} \bar{\sigma}_0^2} \right)^{\frac{1}{3}} \quad \text{for} \quad \frac{|\bar{\sigma}_0|}{\bar{\lambda}} \gg \sqrt{10^{\text{pH} - \text{p}K_a}}, \tag{A10}$$

which is the same as (3.3) in the main text.

REFERENCES

- AJDARI, A. 1995 Electro-osmosis on inhomogeneously charged surfaces. *Phys. Rev. Lett.* **75** (4), 755–758.
 ALIZADEH, A., HSU, W.-L., WANG, M. & DAIGUJI, H. 2021 Electroosmotic flow: from microfluidics to nanofluidics. *Electrophoresis* **42** (7–8), 834–868.
 ARULANANDAM, S. & LI, D. 2000 Determining ζ potential and surface conductance by monitoring the current in electro-osmotic flow. *J. Colloid Interface Sci.* **225** (2), 421–428.
 BALDESSARI, F. 2008 Electrokinetics in nanochannels: Part I. Electric double layer overlap and channel-to-well equilibrium. *J. Colloid Interface Sci.* **325** (2), 526–538.

- BANDOPADHYAY, A., TRIPATHI, D. & CHAKRABORTY, S. 2016 Electroosmosis-modulated peristaltic transport in microfluidic channels. *Phys. Fluids* **28** (5), 052002.
- BAZANT, M. Z. & SQUIRES, T. M. 2004 Induced-charge electrokinetic phenomena: theory and microfluidic applications. *Phys. Rev. Lett.* **92** (6), 066101.
- BEHRENS, S. H. & GRIER, D. G. 2001 The charge of glass and silica surfaces. *J. Chem. Phys.* **115** (14), 6716–6721.
- BROWN, W., KVETNY, M., YANG, R. & WANG, G. 2021 Higher ion selectivity with lower energy usage promoted by electro-osmotic flow in the transport through conical nanopores. *J. Phys. Chem. C* **125** (6), 3269–3276.
- BURGREEN, D. & NAKACHE, F. 1964 Electrokinetic flow in ultrafine capillary slits. *J. Phys. Chem.* **68** (5), 1084–1091.
- CHEN, G. & DAS, S. 2015 Electroosmotic transport in polyelectrolyte-grafted nanochannels with pH-dependent charge density. *J. Appl. Phys.* **117** (18), 185304.
- CHEN, G. & DAS, S. 2017 Massively enhanced electroosmotic transport in nanochannels grafted with end-charged polyelectrolyte brushes. *J. Phys. Chem. B* **121** (14), 3130–3141.
- DAS, S., DUBSKY, P., VAN DEN BERG, A., & EIJKEL, J. C. T. 2012 Concentration polarization in translocation of DNA through nanopores and nanochannels. *Phys. Rev. Lett.* **108** (13), 138101.
- DENG, D., AOUAD, W., BRAFF, W. A., SCHLUMPBERGER, S., SUSS, M. E. & BAZANT, M. Z. 2015 Water purification by shock electro dialysis: deionization, filtration, separation, and disinfection. *Desalination* **357**, 77–83.
- DUAN, M., ZHANG, R., CHEN, J. & CHEN, G. 2024 Influence of salt, confinement and pH on surface ionization. *Phys. Rev. Lett.* (submitted).
- GHOSAL, S. 2004 Fluid mechanics of electroosmotic flow and its effect on band broadening in capillary electrophoresis. *Electrophoresis* **25** (2), 214–228.
- HAYWOOD, D. G., HARMS, Z. D. & JACOBSON, S. C. 2014 Electroosmotic flow in nanofluidic channels. *Anal. Chem.* **86** (22), 11174–11180.
- HUANG, G., WILLEMS, K., SOSKINE, M., WLOKA, C. & MAGLIA, G. 2017 Electro-osmotic capture and ionic discrimination of peptide and protein biomarkers with FraC nanopores. *Nat. Commun.* **8** (1), 935.
- HUI, T. H., KWAN, K. W., YIP, T. T. C., FONG, H. W., NGAN, K. C., YU, M., YAO, S., NGAN, A. H. W. & LIN, Y. 2016 Regulating the membrane transport activity and death of cells via electroosmotic manipulation. *Biophys. J.* **110** (12), 2769–2778.
- HUR, J. & CHUNG, A. J. 2021 Microfluidic and nanofluidic intracellular delivery. *Adv. Sci.* **8** (15), 2004595.
- KOUNOVSKY-SHAFFER, K. L., et al. 2017 Electrostatic confinement and manipulation of DNA molecules for genome analysis. *Proc. Natl Acad. Sci. USA* **114** (51), 13400–13405.
- KOYAMA, S., INOUE, D., OKADA, A. & YOSHIDA, H. 2021 Electro-osmotic diode based on colloidal nanoparticles between double membranes. *Phys. Rev. Res.* **3** (3), 033289.
- LI, J. & LI, D. 2019 Electroosmotic flow velocity in DNA modified nanochannels. *J. Colloid Interface Sci.* **553**, 31–39.
- LIU, B.-T., TSENG, S. & HSU, J.-P. 2015 Analytical expressions for the electroosmotic flow in a charge-regulated circular channel. *Electrochem. Commun.* **54**, 1–5.
- MANNING, G. S. 1967 Model for electro-osmosis in fixed-charge systems. *J. Chem. Phys.* **46** (12), 4976–4980.
- MUELLER, R., KAMMLER, H. K., WEGNER, K. & PRATSINIS, S. E. 2003 OH surface density of SiO₂ and TiO₂ by thermogravimetric analysis. *Langmuir* **19** (1), 160–165.
- PENG, R. & LI, D. 2016 Electroosmotic flow in single PDMS nanochannels. *Nanoscale* **8** (24), 12237–12246.
- PENNATHUR, S. & SANTIAGO, J. G. 2005 Electrokinetic transport in nanochannels. 2. Experiments. *Exp. Anal. Chem.* **77** (21), 6782–6789.
- PICALLO, C. B., GRAVELLE, S., JOLY, L., CHARLAIX, E. & BOCQUET, L. 2013 Nanofluidic osmotic diodes: theory and molecular dynamics simulations. *Phys. Rev. Lett.* **111** (24), 244501.
- SADEGHI, M., SAIDI, M. H. & SADEGHI, A. 2017 Electroosmotic flow and ionic conductance in a pH-regulated rectangular nanochannel. *Phys. Fluids* **29** (6), 062002.
- SCHMID, S., STÖMMER, P., DIETZ, H. & DEKKER, C. 2021 Nanopore electro-osmotic trap for the label-free study of single proteins and their conformations. *Nat. Nanotechnol.* **16** (11), 1244–1250.
- SCHOCH, R. B., HAN, J. & RENAUD, P. 2008 Transport phenomena in nanofluidics. *Rev. Mod. Phys.* **80** (3), 839–883.
- SJÖBERG, S. 1996 Silica in aqueous environments. *J. Non-Crystalline Solids* **196**, 51–57.
- SQUIRES, T. M. & BAZANT, M. Z. 2004 Induced-charge electro-osmosis. *J. Fluid Mech.* **509**, 217–252.
- STONE, H., STROOCK, A. & AJDARI, A. 2004 Engineering flows in small devices: microfluidics toward a lab-on-a-chip. *Annu. Rev. Fluid Mech.* **36** (1), 381–411.

- STOREY, B. D., EDWARDS, L. R., KILIC, M. S. & BAZANT, M. Z. 2008 Steric effects on ac electro-osmosis in dilute electrolytes. *Phys. Rev. E* **77** (3), 036317.
- TREFALT, G., BEHRENS, S. H. & BORKOVEC, M. 2016 Charge regulation in the electrical double layer: ion adsorption and surface interactions. *Langmuir* **32** (2), 380–400.
- VAN DER, H., FRANK, H., BONTHUIS, D. J., STEIN, D., MEYER, C. & DEKKER, C. 2006 Electrokinetic energy conversion efficiency in nanofluidic channels. *Nano Lett.* **6** (10), 2232–2237.
- ZHAO, C. & YANG, C. 2012 Advances in electrokinetics and their applications in micro/nano fluidics. *Microfluid Nanofluid* **13** (2), 179–203.